STRATOCUMULUS-CAPPED MIXED LAYERS DERIVED FROM A THREE-DIMENSIONAL MODEL

JAMES W. DEARDORFF

Department of Atmospheric Sciences, Oregon State University, Corvallis, Oregon 97331, U.S.A.

(Received in final form 23 October, 1979)

Abstract. Results of a three-dimensional numerical model are analysed in a study of turbulence and entrainment within mixed layers containing stratocumulus with or without parameterized cloud-top radiative cooling. The model eliminates most of the assumptions invoked in theories of cloud-capped mixed layers, but suffers disadvantages which include poor resolution and large truncation errors in and above the capping inversion.

For relatively thick mixed layers with relatively thick capping inversions, the cloud-top radiative cooling is found to be lodged mostly within the capping inversion when the cooling is confined locally to the upper 50 m or less of the cloud. It does not then contribute substantially towards increased buoyancy flux and turbulence within the well mixed layer just below.

The optimal means of correlating the entrainment rate, or mixed-layer growth rate, for mixed layers of variable amounts of stratocumulus is found to be through functional dependence upon an overall jump Richardson number, utilizing as scaling velocity the standard deviation of vertical velocity existing at the top of the mixed layer (near the center of the capping inversion). This velocity is found to be a fraction of the generalized convective velocity for the mixed layer as a whole which is greater for cloud-capped mixed layers than for clear mixed layers.

1. Introduction

An atmospheric boundary layer capped by a deck of stratocumulus clouds is a common occurrence over cool portions of oceans and over land behind many cold fronts. Observationally, however, little is known about the structure of the turbulence in this kind of boundary layer in comparison with what is known about the clear, well mixed boundary layer. There are special difficulties in measuring temperature and moisture within clouds using the instrumented aircraft, and only that kind of instrument platform can supply turbulence data which is at all representative of the horizontal mean or ensemble average. Theories of the stratocumulus-capped mixed layer have therefore had little or no reliable quantitative data to guide them. Three-dimensional numerical results are presented here in hopes of providing some small measure of the needed guidance, and to point out special difficulties which future three-dimensional modelers of such mixed layers could try to avoid.

The pioneering theoretical paper on this topic is that of Lilly (1968) who included influences of condensation and evaporation, large-scale vertical motion, and divergence of net irradiance at the cloud top. His major assumptions consisted of:

(a) up to the base of the capping inversion, the boundary layer is well mixed, or uniform, in mean values of semi-conservative properties such as total-moisture specific humidity (q_w) and wet-bulb potential temperature (θ_w) or equivalent potential temperature (θ_e);

Boundary-Layer Meteorology **18** (1980) 495–527. 0006–8314/80/0184–0495. $04.95.

(b) the capping inversion is of negligible thickness;

(c) the upper, cloudy portion of the mixed layer is entirely saturated (no holes of unsaturated air), and the buoyancy flux of entrainment occurs entirely in the saturated air;

(d) none of the turbulence energy that drives the vertical mixing is generated from wind shear, but rather from buoyancy forces;

(e) there is no precipitation or drizzle;

(f) the divergence of net irradiance occurs entirely within the capping inversion, and not at all within the upper mixed layer;

(g) the jump in θ_w or θ_e across the capping inversion ($\Delta\theta_w$ and $\Delta\theta_e$, respectively) must be positive for parcel stability and maintenance of the stratocumulus cloud layer; and

(h) the entrainment rate, or growth rate relative to any mean subsidence, of the mixed layer is bounded on the upper side by that which can be deduced if there were no dissipation (Ball's (1960) assumption of 'maximum' entrainment), and on the lower side by the value that can be deduced if the buoyancy flux were just zero at some height within the mixed layer and positive at all other heights within the mixed layer ('minimum' entrainment rate).

With these assumptions, and with cloud-top divergence of net irradiance and large-scale subsidence both being present and important, Lilly showed that the height reached by the marine mixed layer under steady conditions did not depend critically upon closure assumption (h).

The next study on this topic was by Schubert (1976), who retained assumptions (a)–(f), and selected a particular closure assumption compatible with (h) that permitted Lilly's theory to be applied quantitatively and generally. His closure assumption is a linear interpolation of the maximum and minimum entrainment-rate assumptions which, in the case of a clear mixed layer, reduces to the common assumption that the entrainment buoyancy flux is $-k$ of the surface buoyancy flux, where k is a constant of order 0.2. He showed that this model produces stratocumulus-capped mixed layers of reasonable structure, and predicted that even over the ocean the diurnal variation of solar radiation should produce significant diurnal variation of mixed-layer depth and cloud-base height.

About the same time, Deardorff (1976a) proposed some revisions to Lilly's theory. In place of assumption (f), he allowed only a fraction r ($0 \leqslant r \leqslant 1$) of the cloud-top divergence in net irradiance to occur within the capping inversion, and the remaining fraction $1-r$ to occur within the uppermost mixed layer just below the capping inversion. In this way, the finite depth of the region over which cloud-top cooling occurs was permitted to provide both enhanced turbulence energy and a cooling tendency within the mixed layer. He utilized $r = 0.5$ in lieu of quantitative information of its value. For an entrainment closure assumption, he took the negative buoyancy flux of entrainment to be -0.5 of the vertically integrated

buoyancy flux throughout the mixed layer. This assumption is the same as Schubert's when the level of minimum buoyancy flux occurs at the base of the capping inversion, and when $r = 1$. Otherwise, it is quite different. In most of the examples treated by Schubert, the minimum buoyancy flux occurred either at cloud base or at the surface.

Examples of stratocumulus-capped mixed layers calculable from Schubert's (1976) model were derived by Kraus and Schaller (1978a). They continued to assume that $r = 1$ and to require the capping inversion to be of zero thickness. Hence, they found the minimum buoyancy flux in cloud-capped cases to occur usually at cloud base, with no negative buoyancy flux of entrainment occurring unless over a layer of zero thickness – their capping inversion. Later, they (Kraus and Schaller, 1978b) recommended use of the closure assumption that the vertically integrated buoyancy flux in layers where it is negative be $-r'$ of the vertically integrated buoyancy flux in layers where it is positive, with r' being of order 0.06. As will be noted later, however, the magnitude of the negative buoyancy flux area depends critically upon assumptions on the detailed placement of the radiative cooling at cloud top and upon details of the mean structure within a capping inversion of finite thickness.

A one-dimensional model with second-moment equations was utilized by Oliver *et al.* (1978) to study stratocumulus within shallow mixed layers. Among their closure assumptions, however, was the requirement that the turbulent transport be directed down the gradient of turbulence energy, a particularly inaccurate assumption for the buoyancy driven, clear mixed layer (André *et al.*, 1976; Zeman and Lumley, 1976) and of questionable accuracy for a cloud-filled mixed layer. The magnitudes of the entrainment rate, entrainment fluxes, capping inversion mean thickness, and vertical gradients of turbulent fluxes within the mixed layer depend upon this assumption. In contrast to earlier models, however, their model did yield a finite depth for the mean capping inversion or cloud-top layer. The resultant cloud-top radiative cooling was found to occur mostly within the upper well-mixed layer.

In a recent paper by Kahn and Businger (1979) it is argued, regarding assumption (*f*), that essentially all the cloud-top divergence of net irradiance should be placed within the mixed layer ($r = 0$) and none within the capping inversion. Their arguments include the fact that all the cloudy air lies within the *local* mixed layer, and that the zone of long-wave radiative cooling can be estimated to extend down below cloud top a relatively large distance of order 100 m.

In a study by Albrecht *et al.*, (1979), 82% of the cloud-top radiative cooling is found to occur in the upper 5 mb (or 50 m) of a cloud having 0.5 g m^{-3} liquid water content. If the distance between uppermost cloud-top domes and lowermost cloud-top cusps were 50 m (which would then correspond closely to the mean capping inversion thickness), if cloud fraction within this layer varied linearly with height between 1 and 0, and if cloud liquid-water content were as large near the cusps as within the domes, over 41% of the cloud-top cooling would still occur within the capping inversion. Thus, it does not appear reasonable to assume that all of it occurs in either the well-mixed layer or the capping inversion alone.

Recent studies by Deardorff (1979) and Randall (1979) investigate assumption (g). They find that because of the influence of liquid-water loading, significantly negative values of $\Delta\theta_w$ and $\Delta\theta_e$ must occur before parcels entraining down into the cloud layer become dynamically unstable. Deardorff calls this instability 'cloud-top entrainment instability' while Randall calls it 'conditional instability of the first kind upside down (CIFKU)'.

The three-dimensional numerical calculations to be examined do not make assumptions (a), (b), (c), (d), (f), (g), or (h), and thus offer the possibility of considerable insight into present uncertainties. However, because of the model's truncation errors, limited horizontal domain, and subgrid-scale flux and cloud-saturation assumptions, its results will need to be interpreted just as carefully as any set of observational data.

2. The Numerical Model

The three-dimensional model is very similar to the one utilized by Deardorff (1974a). It is a physical-space model above a uniform, horizontal surface with 40 grid intervals in each of the three coordinate directions. The vertical grid increment, Δz, was 50 m in all cases; in two 'dry cloud' cases $\Delta x = \Delta y = 125$ m, and in the real cloud simulations it was found necessary to reduce this to $\Delta x = \Delta y = 50$ m. In the latter cases the physical domain was thus a 2 km cube in which the mixed layer usually had a height between 1 and 1.5 km.

2.1. Governing equations

The model equations are as follows: For momentum,

$$\frac{\partial \bar{u}}{\partial t} = -\frac{\partial}{\partial x}(\bar{u}^2 + \overline{u'^2} - \tfrac{2}{3}\bar{E}) - \frac{\partial}{\partial y}(\bar{u}\bar{v} + \overline{u'v'}) - \frac{\partial}{\partial z}(\bar{u}\bar{w} + \overline{u'w'}) -$$

$$-\frac{\partial}{\partial x}(\bar{p}/\rho_0 + \tfrac{2}{3}\bar{E}) + 2\Omega_z\bar{v} - 2\Omega_y\bar{w} \tag{1a}$$

$$\frac{\partial \bar{v}}{\partial t} = -\frac{\partial}{\partial x}(\bar{u}\bar{v} + \overline{u'v'}) - \frac{\partial}{\partial y}(\bar{v}^2 + \overline{v'^2} - \tfrac{2}{3}\bar{E}) - \frac{\partial}{\partial z}(\bar{v}\bar{w} + \overline{v'w'}) -$$

$$-\frac{\partial}{\partial y}(\bar{p}/\rho_0 + \tfrac{2}{3}\bar{E}) - 2\Omega_z\bar{u} \tag{1b}$$

$$\frac{\partial \bar{w}}{\partial t} = -\frac{\partial}{\partial x}(\bar{u}\bar{w} + \overline{u'w'}) - \frac{\partial}{\partial y}(\bar{v}\bar{w} + \overline{v'w'}) - \frac{\partial}{\partial z}(\bar{w}^2 + \overline{w'^2} - \tfrac{2}{3}\bar{E} -$$

$$-\langle \bar{w}^2 + \overline{w'^2} - \tfrac{2}{3}\bar{E}\rangle) -$$

$$-\frac{\partial}{\partial z}(\bar{p}/\rho_0 + \tfrac{2}{3}\bar{E} - \langle \bar{p}/\rho_0 + \tfrac{2}{3}\bar{E}\rangle) + 2\Omega_y(\bar{u} - \langle \bar{u}\rangle) +$$

$$+\frac{g}{\theta_0}(\bar{\theta}_v - \langle \bar{\theta}_v\rangle). \tag{1c}$$

In (1), the x axis points east and y north; overbars signify the Reynolds average over the volume $\Delta x \cdot \Delta y \cdot \Delta z$ (or somewhat in excess of this volume) and centered at the point under consideration, and primes signify the local deviations therefrom. The horizontal average is denoted by the angular brackets, $\langle\ \rangle$. Equation (1c) has the hydrostatic and residual mean values (horizontally averaged) subtracted away so $\langle \partial \bar{w}/\partial t \rangle = 0 = \partial \langle \bar{w} \rangle / \partial t = \langle \bar{w} \rangle$ when cyclic lateral boundary conditions are used. Also, Ω_y, Ω_z are components of the earth's angular velocity; ρ_0 and θ_0 are constant reference values of density and potential temperature, p is pressure, g is the gravitational acceleration appearing in the Boussinesq buoyancy term, and $\bar{E}$ is the subgrid-scale turbulence energy ($\bar{E} = \frac{1}{2}(\overline{u'^2} + \overline{v'^2} + \overline{w'^2})$). A latitude of $-34.5°$ was specified, and the large-scale geostrophic wind involving $\partial \langle \bar{p} \rangle / \partial y$ was taken to be constant with height and time and directed from east to west with a magnitude of 5.5 m s^{-1}.

In the buoyancy term, θ_v is the virtual potential temperature defined by

$$\theta_v = \theta(1 + 0.61q - q_l) \tag{2}$$

where the specific humidity is q and the specific liquid-water content is q_l.

For the thermodynamic variable, Betts' (1973) liquid-water potential temperature, θ_l, was employed. Its linearized version is defined by

$$\theta_l = \theta - \left(\frac{L}{c_p}\frac{\theta}{T}\right) q_l \tag{3}$$

where L is the latent heat of vaporization, c_p is the specific heat at constant pressure, and T is the absolute temperature. For shallow cloud convection with no precipitation, θ_l is conserved to the extent that $(L/c_p)\,(\theta/T)$ is essentially constant. A convenience of utilizing θ_l is that it becomes the same as θ in clear air ($q_l = 0$). The governing equation for θ_l that was utilized is:

$$\frac{\partial \bar{\theta}_l}{\partial t} = -\frac{\partial}{\partial x}(\bar{u}\bar{\theta}_l + \overline{u'\theta'_l}) - \frac{\partial}{\partial y}(\bar{v}\bar{\theta}_l + \overline{v'\theta'_l} - \frac{\partial}{\partial z}(\bar{w}\bar{\theta}_l + \overline{w'\theta'_l}) - \frac{\partial F}{\partial z} \tag{4}$$

where F is the net irradiance normalized by density and specific heat. The radiative warming rate, $-\partial F/\partial z$, was set to zero generally except near cloud top where it was given a value of -1.5×10^{-3} K s^{-1}. This value corresponds to an increase in net kinematic radiative flux of 0.075 m s^{-1} K over a depth of 50 m.

The governing equation for the total specific humidity, $q_w = q + q_l$, that was utilized is:

$$\frac{\partial \bar{q}_w}{\partial t} = -\frac{\partial}{\partial x}(\bar{u}\bar{q}_w + \overline{u'q'_w}) - \frac{\partial}{\partial y}(\bar{v}\bar{q}_w + \overline{v'q'_w}) - \frac{\partial}{\partial z}(\bar{w}\bar{q}_w + \overline{w'q'_w}) . \tag{5}$$

In the absence of precipitation, q_w is conserved.

For purposes of determining θ_v and the presence or absence of cloud, the parameterization of Deardorff (1976b) was employed to obtain $\bar{\theta}$, $\bar{q}$ and $\bar{q}_l$, given $\bar{\theta}_l$, $\bar{q}_w$ and $\langle \bar{p} \rangle$. If a grid volume was found to be saturated, it was assumed to be uniformly

saturated throughout the grid volume. The numerical calculations were performed before the parameterizations for variable subgrid-scale condensation (Sommeria and Deardorff, 1977; Mellor, 1977; Oliver *et al.*, 1978) were developed.

2.2. Subgrid-scale fluxes and dissipation

Representation of the subgrid-scale turbulent fluxes was accomplished through a much simpler method than in Deardorff (1974a). Eddy-coefficient relations were employed for fluxes of semi-conservative quantities, and the subgrid-scale eddy coefficient was made proportional to the square root of the subgrid-scale turbulence intensity, $\bar{E}$. The latter is governed by

$$\frac{\partial \bar{E}}{\partial t} = -\frac{\partial}{\partial x_i}(\bar{u}_i \bar{E}) - \overline{u_i' u_j'} \frac{\partial \bar{u}_i}{\partial x_j} + \frac{g}{\theta_0} \overline{w' \theta_v'} - \frac{\partial}{\partial x_i}[\overline{u_i'(e' + p'/\rho_0)}] - \varepsilon \tag{6}$$

where $e' \equiv \frac{1}{2}(u'^2 + v'^2 + w'^2)$ and ε is the rate of dissipation within the grid volume. The subgrid fluxes were parameterized by

$$\overline{u_i' u_j'} = -K_m(\partial \bar{u}_i/\partial x_j + \partial \bar{u}_j/\partial x_i) + (2/3)\delta_{ij}\bar{E} \tag{7a}$$

$$\overline{u_i' \theta_l'} = -K_h \partial \bar{\theta}_l/\partial x_i \tag{7b}$$

$$\overline{u_i' q_w'} = -K_h \partial \bar{q}_w/\partial x_i \tag{7c}$$

$$\overline{u_i' \theta_v'} = \overline{A u_i' \theta_l'} + B\bar{\theta}\, \overline{u_i' q_w'} \tag{7d}$$

$$\overline{u_i'(e' + p'/\rho_0)} = -2K_m \partial \bar{E}/\partial x_i \tag{7e}$$

where K_m is a subgrid-scale eddy coefficient for momentum, K_h is a subgrid eddy coefficient for scalar quantities and A, B are approximate constants which, in unsaturated air are given by

$$A = 1 + 0.61\bar{q}_w \qquad B = 0.61 \tag{8a}$$

and in saturated air by

$$A = (1 + 0.61 q_w) - E_3\left[\frac{L}{c_p \bar{T}}(1 + 0.61 q_w) - 1.61\right]; \qquad B = \frac{L}{c_p \bar{T}} - 1\,. \tag{8b}$$

In (8b), E_3 is given by (see Deardorff, 1976a)

$$E_3 = 0.622 \frac{L}{R\bar{T}} \bar{q}_s \Big/ \left[1 + 0.622 \frac{L}{R\bar{T}} \frac{L}{c_p \bar{T}} \bar{q}_s\right] \tag{8c}$$

where R is the gas constant for air and q_s the saturation specific humidity.

The subgrid-scale eddy coefficients in (7) were assumed given by

$$K_m = 0.10 l \bar{E}^{1/2} \tag{9a}$$

$$K_h = (1 + 2l/\Delta s) K_m \tag{9b}$$

where

$$\Delta s = (\Delta x \cdot \Delta y \cdot \Delta z)^{1/3} \tag{9c}$$

and l is a subgrid-scale mixing length which was required not to exceed the grid scale, Δs, in magnitude. In past work it has been assumed that $l = \Delta s$, which fails to take account of the possibility that in a stably stratified region l could become much smaller than the grid interval. Here it was assumed that

$$l = l_s = 0.76\bar{E}^{1/2}\left(\frac{g}{\theta_0}\frac{\partial\bar{\theta}_l}{\partial z}\right)^{-1/2} \tag{10a}$$

when $\partial\bar{\theta}_l/z > 0$ and $l_s < \Delta s$. Otherwise, it was assumed that

$$l = \Delta x\,. \tag{10b}$$

Hence, (9) gives $K_h/K_m = 1$ as a lower limit in very stable conditions, and a value of 3 as an upper limit in neutral and unstable stratification. It should be emphasized that for scales of motion greater than 50 or 100 m, no eddy coefficients were utilized in obtaining the vertical fluxes, and derivable eddy coefficients for the flow as a whole at a given height were not constrained by (9a,b).

Since the criterion $\partial\bar{\theta}_l/\partial z < 0$ marks the onset of parcel instability whether the parcel and surroundings are totally saturated or totally unsaturated, this quantity appearing on the right side of (10a) is a satisfactory stability indicator for use on the subgrid scale in this study.

Typical values of l within the mixed layer were between 40 and 50 m, while in the center of the capping inversion, (10a) caused l to become as small as 3 m. Interestingly, formulations (9), (10) can permit the net subgrid-scale flux to be countergradient in the following manner. In local regions where $\partial\bar{\theta}_l/\partial z < 0$, the subgrid-scale flux $\overline{w'\theta_l'}$, for example, is positive and tends to be relatively large; in other regions at the same height and time where $\partial\bar{\theta}_l/\partial z > 0$, the flux is downward but small, since l is smaller than Δs there, and K_h is smaller too. The net result can be an upward directed flux of θ_l' when $\partial\bar{\theta}_l/\partial z$ is slightly positive in the mean.

The dissipation rate, ε in (6), was assumed given by

$$\varepsilon = C\bar{E}^{3/2}/l \tag{11a}$$

where

$$C = 0.19 + 0.51l/\Delta s\,. \tag{11b}$$

Close to the surface, however, C was increased by a 'wall-effect' factor of up to 3.9 to prevent $\bar{E}$ from becoming unduly large there. In (11b) $C \to 0.19$ in the stable limit, for which case it can be shown that this parameterization yields a critical gradient Richardson number (when only the $\partial\bar{u}/\partial z$ or $\partial\bar{v}/\partial z$ component of shear is present) for subgrid-scale turbulence of 0.23.

In actual use, (6) was divided through by $2\bar{E}^{1/2}$ and converted to an equation for $\partial\bar{E}^{1/2}/\partial t$. In so doing, the triple correlation term, or flux divergence term, was altered slightly from

$$\frac{1}{2\bar{E}^{1/2}}\frac{\partial}{\partial x_i}\left(2K_m\frac{\partial\bar{E}}{\partial x_i}\right) \quad \text{to} \quad \frac{\partial}{\partial x_i}\left(2K_m\frac{\partial\bar{E}^{1/2}}{\partial x_i}\right)$$

in order to preserve a divergence form. This use of $\bar{E}^{1/2}$ avoided the necessity of taking square roots in calculating K_m and ε at each grid point.

2.3. Boundary and initial conditions

These were treated about the same as described by Deardorff (1974a). In particular, at $z = 2$ km

$$\bar{w} = 0 = \frac{\partial \bar{u}}{\partial z} = \frac{\partial \bar{v}}{\partial z} = \frac{\partial \bar{E}^{1/2}}{\partial z};$$
$$\bar{\theta}_l(2\text{ km}) = \bar{\theta}_l(1.95\text{ km}) + [\partial \langle \bar{\theta}_l \rangle \partial z\,(1.925\text{ km})]\Delta z$$
$$\bar{q}_w(2\text{ km}) = \bar{q}_w(1.95\text{ km}) + [\partial \langle \bar{q}_w \rangle / \partial z\,(1.925\text{ km})]\Delta z\,. \tag{12}$$

At $z = 0$, $\bar{w} = 0$; there the subgrid-scale fluxes were prescribed from bulk aerodynamic surface-layer formulas utilizing properties at 25 or 50 m and at the surface where a roughness length of 1 cm was specified. Surface-layer stratification was taken into account according to Obukhov similarity principles as quantified by Businger *et al.*, (1971). Surface temperature and specific humidity were assumed constant in the horizontal. The former was diagnosed from a surface energy balance and 12 soil levels of temperature; solar radiation was specified for the simulated latitude for the month of August as a function of time of day for clear skies, except as attenuated by 65% when stratocumulus was present. Surface specific humidity was diagnosed from Manabe's (1969) simple equation which relates it to net soil moisture and humidity within the surface layer.

Lateral boundary conditions were cyclic, except for pressure which had a geostrophic trend along the y axis. The average surface pressure was held constant at 1022 mb.

Initial conditions consisted of three-dimensional fields of $\bar{u}_i$, $\bar{\theta}_l$, $\bar{q}_w$ and $\bar{E}^{1/2}$ existing on tape at the ends of earlier numerical integrations. Before each new case, these were altered in horizontal mean temperature and moisture content so that stratocumulus of a desired thickness and cloud-top height would subsequently form. In any given numerical integration or case, a time period of from $\frac{1}{2}$ to 1 h was allowed to elapse after the altered initial conditions before statistics of the boundary-layer turbulence were collected for analysis.

2.4. Finite-difference methods

The space-staggered grid of Lilly (1965) and of Arakawa (1966) was utilized in conjunction with quadratic-conserving spatial finite differences of second-order accuracy. In this grid system, values of $\bar{p}$ and $\bar{E}^{1/2}$ are located at heights of $\frac{1}{2}\Delta z$, $\frac{3}{2}\Delta z, \ldots$; values of $\bar{u}_i$ are at the same locations except being displaced $\pm\frac{1}{2}\Delta x_i$. The scalars $\bar{\theta}_l$ and $\bar{q}_w$ were positioned at the same locations as $\bar{w}$ so that the buoyancy term would be compactly represented; the heights of $\bar{w}$ grid levels were 0, Δz, $2\Delta z, \ldots$.

Time differencing was by the Adams–Bashforth method wherein

$$\bar{u}_i(\mathbf{x}, n+1) = \bar{u}_i(\mathbf{x}, n) + \Delta t\left[\frac{3}{2}\frac{\partial \bar{u}_i}{\partial t}(\mathbf{x}, n) - \frac{1}{2}\frac{\partial \bar{u}_i}{\partial t}(\mathbf{x}, n-1)\right]$$

where n is the time index and Δt the time step. The latter had values ranging between 3 and 5 s.

The effective pressure term in (1), namely $\bar{p}/\rho_0 + \frac{2}{3}\bar{E}$, was obtained diagnostically from an exact solution of the finite-difference Poisson equation obtained from the finite-difference divergence of (1). This solution preserved the condition of incompressibility, $\partial \bar{u}_i/\partial x_i = 0$, centered at each pressure grid point.

The numerical program executed about 6 times slower than real time on the CDC 7600 computer.

3. Cases Treated

All cases may be compared against the Australian Wangara Experiment for day 33 (Clarke *et al.*, 1971) as simulated by Deardorff (1974a,b) with a similar numerical model. Skies were clear in this case, which will be designated Case 1.

Cases 2 and 3 simulate Lilly's (1968) 'dry cloud' which contains no liquid-vapor phase changes but does contain long-wave radiative cooling at its top. This might simulate a cloud of dense smoke, and serves to illustrate the potential importance of cloudtop cooling while avoiding complications associated with the presence of liquid water. The radiative cooling was prescribed in these two cases to occur at a single, constant height located just inside the top of the mixed layer. Case 2 was accompanied by a moderately strong surface turbulent heat flux, and Case 3 with an extremely weak one (see Table I).

The 4th case is for a stratocumulus deck occupying the upper half of the mixed layer with liquid-water effects included but with radiative effects omitted.

The 5th case is the same except that the capping inversion was very weak, the cloud top was unstable for downward penetrating parcels, and entrainment occurred very rapidly. The earlier evolution of this case is described in Deardorff (1980).

The 6th case is the same as case 4 except that cloud-top radiative flux divergence was prescribed to be present at the uppermost grid volume in each vertical column for which $\bar{q}_l$ exceeded 0.01×10^{-3}. Thus, the radiative flux divergence occurred over only the uppermost 50 m of cloud, while the cloud-top height varied somewhat in space and time.

Case 7 is the same as Case 6 except that the cloud occupied almost the entire mixed layer instead of just its upper half.

A brief characterization of these 7 cases is presented in Table I. Average mixed-layer or cloud-top height is designated by h, cloud-base height by h_b, surface turbulent heat flux by $\langle w\theta \rangle_s$, surface moisture flux by $\langle wq \rangle_s$, bulk soil moisture fraction (with respect to a saturated soil with the potential evaporation rate) by W, soil surface potential temperature by θ_s, and specific humidity at the surface by q_{sfc}.

TABLE I

Descriptive properties of the 7 cases

Case	Time Period	h (m)	h_b (m)	Phase Change	Cloudtop Radiative Cooling	$\langle w\theta \rangle_s$ (mm s^{-1} K)	$\langle wq \rangle_s$ (mm s^{-1} g/kg)	W	θ_s(K)	q_{sfc} (g/kg)
1	13.37 to 13.43 hr (1-3)	1300	–	No	No	198	23	0.10	300.2	5.0
2	13.31 to 13.50 hr (10)	1200	–	No	Yes	99	15	0.10	289.0	3.85
3	14.24 to 14.78 hr (10)	1220	–	No	Yes	3	5	0.10	283.8	3.46
4	14.35 to 14.80 hr (10)	1400	780	Yes	No	89	10	0.09	286.2	5.82
5	16.32 hr (1)	1795	990	Yes	No	38	6	0.09	284.8	5.70
6	14.44 to 14.98 hr (10)	1160	620	Yes	Yes	73	22	0.30	285.7	6.85
7	16.52 to 16.90 hr (10)	1550	200	Yes	Yes	27	7	0.70	284.2	8.02

The numbers in parenthesis under the entries in the time-period column refer to the number of elements or individual data sets that were averaged to obtain ensemble-average vertical profiles.

4. Mean Profiles of Temperature, Moisture, and their Vertical Fluxes

4.1. Clear-sky case 1

Vertical profiles of $\langle \bar{\theta}_v \rangle$, $\langle \overline{w\theta_v} \rangle$, and $\langle \overline{wq} \rangle$ taken from Deardorff (1974a) are shown in Figure 1. The fluxes include the subgrid-scale contributions, since, for example,

$$\langle \overline{w\theta} \rangle = \langle \bar{w}\bar{\theta} \rangle + \langle \overline{w'\theta'} \rangle .$$

Because of entrainment, there is a negative flux of θ_v at the top of the mixed layer and a positive flux of q in approximate accordance with the relations (see Lilly, 1968):

$$\langle w\theta_v \rangle_h = -w_e \Delta\theta_v \tag{13a}$$

$$\langle wq \rangle_h = -w_e \Delta q \tag{13b}$$

where w_e is the entrainment rate and $\Delta\theta_v$ and Δq are jumps in property across the capping inversion, or entrainment layer, which in this case extends from about 1200

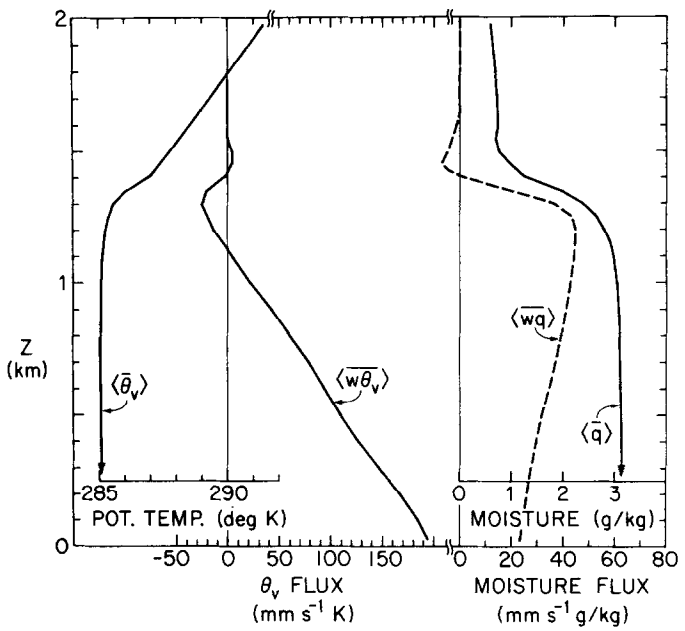

Fig. 1. Vertical profiles of (horizontally averaged) virtual potential temperature (θ_v) and its vertical flux, and specific humidity (q) and its vertical flux, for Case 1.

to 1400 m. These jump relations are derived under the assumptions that the capping inversion is infinitesimal in thickness, the air beneath is fully mixed, and the air above is non-turbulent.

As mentioned in Deardorff (1974a), the negative moisture flux occurring just above the capping inversion in this and subsequent cases, and also the weak positive heat flux at the same height, are believed to be spurious, or mostly spurious. They lie in a region where internal gravity-wave motions calculated by the model are poorly resolved and dominated by truncation errors. No physical mechanism to explain the anomalous negative moisture flux has yet been conceived, and the moisture-flux divergence between 1.5 and 1.6 km is seen to have almost caused the air in this layer to become drier than at surrounding heights.

4.2. Dry-cloud cases

Profiles of the same four quantities for Cases 2 and 3 are shown in Figures 2 and 3, respectively. There is now a very substantial positive buoyancy flux near the top of the mixed layer, at $z = 1125$ m in these two cases, because of the radiative cooling inserted just above there. The heights where the cooling was applied are shown in the two figures. This cooling in the upper mixed layer leads to a positive buoyancy flux there for the same reason that heating at the bottom of a mixed layer leads to a positive buoyancy flux there. Thus, mixed-layer turbulence could be maintained equally well by either or both of these mechanisms.

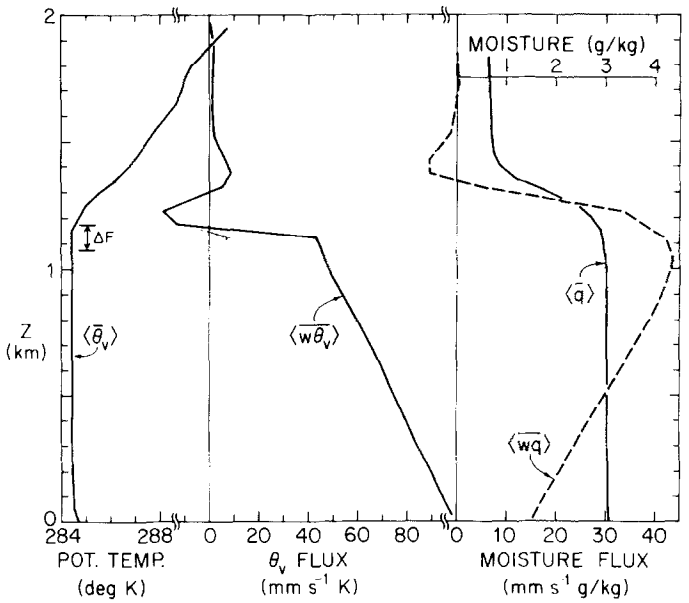

Fig. 2. Vertical profiles of mean virtual potential temperature and its vertical flux, and specific humidity and its vertical flux, for Case 2. The imposed dry-cloud radiative cooling was positioned between the arrowheads at the left.

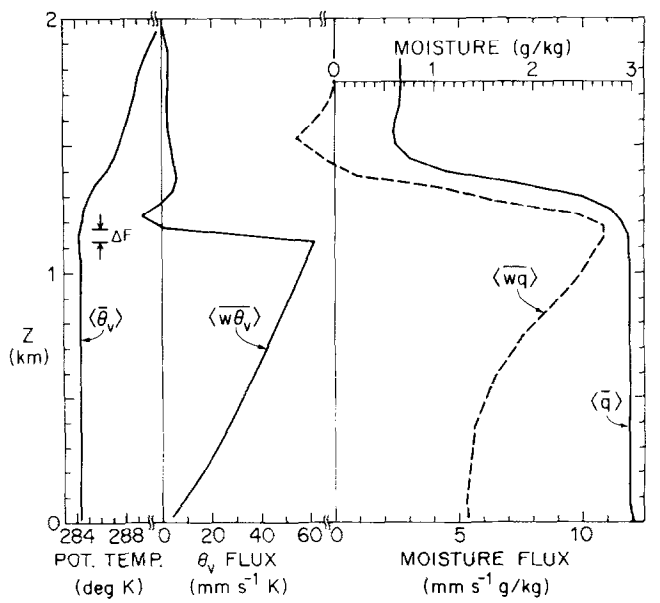

Fig. 3. Vertical profiles of mean virtual potential temperature and its vertical flux, and specific humidity and its vertical flux, for Case 3. The imposed dry-cloud radiative cooling was located between the arrows on the left.

Entrainment again occurs, so that a negative buoyancy flux of entrainment exists just above the layer of radiative cooling, producing a 'double-jump' structure in $\langle w\theta_v \rangle$. If the radiative cooling had instead been applied at a slightly greater height entirely within the capping inversion, its effect would have been to cool the capping inversion layer and thus to promote entrainment indirectly by reshaping the temperature profile there. (Kahn and Businger (1979) refer to this process as 'direct' entrainment.) Then the lower jump in $\langle w\theta_v \rangle$ just below the entrainment layer would not have occurred. Probably both effects occur at the top of an actual stratocumulus-capped mixed layer, though mesoscale variations could obscure or smooth out the double jump.

Cases 2 and 3 exhibit only slight capping inversions in that $\Delta\theta_v$ across the entrainment layer of depth Δh only slightly exceeds $(\partial\theta_v/\partial z)^+ \Delta h$, where the plus superscript indicates evaluation just above the capping inversion. This seemingly unrealistic feature is believed to be a result of having forced the strong radiative cooling to occur at a fixed height which turned out to be about 100 m too low.

The curvature in the $\langle \overline{wq} \rangle$ profile of Figure 3 reflects insufficient sampling. During the period analyzed, this 2 km by 2 km section of the mixed layer was becoming slightly drier in its upper half relative to its lower half (compare this $\langle \overline{wq} \rangle$ profile with that of Figure 2).

Profiles of the kinematic net upward radiative flux are shown in Figure 4. Using (4), these were obtained from

$$F(z) = F(0) + \langle \overline{w\theta_l} \rangle_0 - \langle \overline{w\theta_l} \rangle - \int_0^z \left\langle \frac{\partial \overline{\theta_l}}{\partial t} \right\rangle \mathrm{d}z'' \tag{14}$$

where $F(0)$, the radiative flux at the surface, was for convenience set to zero; z'' is a dummy height variable. The positive jump in radiative flux near the top of the mixed layer in Cases 2 and 3 approximately balances the negative jump in $\langle w\theta_v \rangle$ at the same height. Imbalances (to be discussed later for Cases 6 and 7) are a measure of integration errors since $\partial F/\partial z$ was specified.

4.3. Moist-cloud cases, no radiative flux

Cases 4 and 5 are in this category. For these cases, Figures 5 and 6 depict not only the profiles of $\langle \bar{\theta}_v \rangle$, $\langle \overline{w\theta_v} \rangle$, $\langle \bar{q}_w \rangle$, and $\langle \overline{wq_w} \rangle$, but also profiles of $\langle \bar{\theta}_l \rangle$, $\langle \overline{w\theta_l} \rangle$, $\langle \bar{q}_l \rangle$, $\langle \overline{wq_l} \rangle$, and the cloud cover, σ_c (fractional saturated area at any given height).

The cloud base is not abrupt, on the horizontal average or ensemble average, but is spread over a height range of 100–150 m. This feature exists at any one time and is not an artifice of the time smoothing, since only 10–20 m changes in h_b (and h also) occurred during the 27-min averaging period utilized to derive the curves in Figure 5, and no time averaging was employed for Figure 6.

Referring first to Figure 5, the $\langle \bar{\theta}_v \rangle$ and $\langle \bar{\theta}_l \rangle$ profiles appear as expected, since in the fully saturated cloud layer the lapse rate is essentially moist adiabatic. The $\langle \overline{w\theta_v} \rangle$

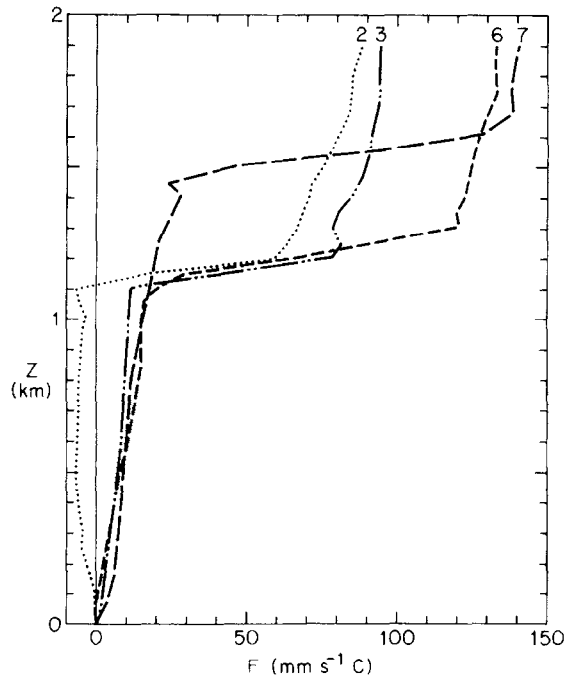

Fig. 4. Vertical profiles of net irradiance normalized by $\rho_0 c_p$, or of the kinematic radiative flux F, for Cases 2, 3, 6 and 7 as deduced from Equation (14).

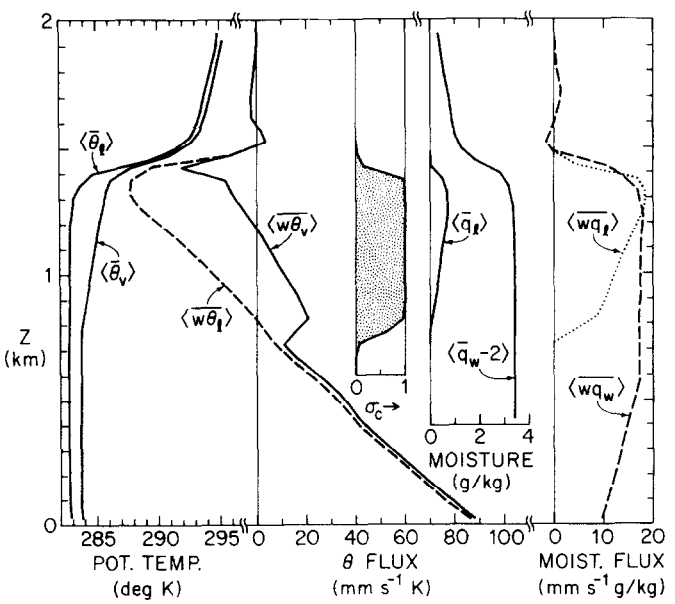

Fig. 5. Vertical profiles of mean liquid-water potential temperature (θ_l) and its vertical flux, virtual potential temperature and its vertical flux, cloud fraction (σ_c) at a given height (stippled area), total specific moisture (q_w) and its vertical flux, and liquid-water specific humidity (q_l) and its vertical flux, for Case 4. Note that 2×10^{-3} is subtracted from $\langle\bar{q}_w\rangle$.

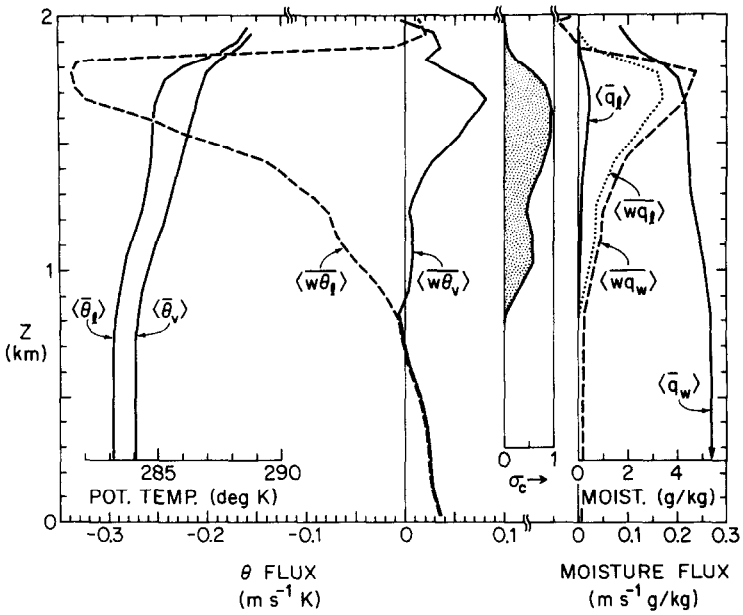

Fig. 6. Vertical profiles of mean liquid-water potential temperature and its vertical flux, virtual potential temperature and its vertical flux, cloud fraction at a given height (stippled area), total specific moisture and its vertical flux, and liquid-water specific humidity and its vertical flux, for Case 5 of rapid entrainment.

profile shows enhanced buoyancy flux in the cloud layer, as deduced by Lilly (1968) and Schubert (1976). However, it also exhibits the negative flux of entrainment in the capping inversion (at $z = 1425$ m in this case), a feature missed by these models which shrink this layer to zero thickness. Near the base of the capping inversion ($z = 1375$ m) where the air consists mostly of cloud elements, this buoyancy flux shifts rather abruptly from negative above to positive below because of evaporative cooling and cloud buoyancy. Thus, the $\langle w\theta_v\rangle$ profile exhibits a double-jump structure even in the absence of cloud-top radiative cooling. Because of the conservative nature of θ_l, however, the $\langle w\theta_l\rangle$ profile does not undergo the lower half of the double jump (though it may if radiative flux divergence is present and extends down into the upper mixed layer).

In Figure 5, $\langle\bar{q}_l\rangle$ increases at the adiabatic rate above the base of the solid cloud cover, until the height is reached above which $\langle\bar{q}_w\rangle$ is not thoroughly mixed, due to entrainment and interception of unmodified air by the horizontal average. The vertical flux of q_l is seen to exceed that of q (vapor) throughout the upper $\frac{3}{4}$ of the cloud layer. As pointed out by Randall (1979), this behavior is not implausible even though $\langle q\rangle$ greatly exceeds $\langle q_l\rangle$. Using a different argument than he did, we may note that in the cloud

$$q_l'' = q_w'' - q_s'' = q_w'' - \frac{\partial q_s}{\partial T} T'' \tag{15}$$

where the double prime is defined by

$$( )'' \equiv ( ) - \langle ( ) \rangle \tag{16}$$

and is the departure from the horizontal mean. Although the two terms on the far right of (15) are the same order of magnitude in the root-mean-square sense, q_w'' (and therefore q_l'') correlates strongly with w while T'' correlates only weakly. That is because $\langle wT'' \rangle$ is closely related to the buoyancy flux which is relatively small in the upper cloud layer (see Figure 5), especially near its zero cross-over height. On the other hand, $\langle wq_w'' \rangle$ remains large at that height.

Case 5 (Figure 6) is Case 4 about two hours later, except that temperatures above $z = h$ had been artificially lowered, gradually, by about 5 °C in the interim so that the capping inversion would be very weak. The entrainment then proceeded much more rapidly, and the fluxes of θ_l, q_w and q_l in the upper mixed layer or upper cloud layer are seen to be hugely enhanced. The entraining air in this instance was cooled sufficiently by evaporation of droplets into it to become unstable, and no definite region of negative $\langle w\theta_v \rangle$ appeared in the upper mixed layer or capping inversion.

The entrainment was sufficiently rapid in Case 5 to cause the cloud cover to be less than 100%, and the cloud gaps were most prevalent in the lower half of the cloud layer. This distribution of cloud cover is consistent with cooled, entraining cloud parcels with lesser q_l values sinking down to the lower part of the cloud layer where they evaporate completely at some height above mean cloud-base height, while rising cloud air continually mushrooms out near cloud top and tends to close up the gaps where entrainment had occurred. Observations of local cloud fraction within a breaking stratocumulus layer undergoing entrainment instability are not available for confirmation.

4.4. Moist cloud cases with radiative flux

Cases 6 and 7 (see Table I) are in this category. The profiles of Case 6 are shown in Figure 7; they resemble closely those of Figure 5 (Case 4) except for greater positive buoyancy flux in the upper half of the cloud layer. It might be thought that this is caused by radiative cooling in the upper mixed layer. However, a comparison of the moisture flux profiles, along with examination of (7d) as applied to the vertical flux of the total turbulence, indicates that increased moisture flux in Case 6 is almost entirely responsible for the increased buoyancy flux over that of Case 4 in the cloud layer. As seen from Table I, the increased moisture flux was a result of increased soil moisture content utilized in Cases 6 and 7.

In Case 6 the zone in which radiative flux divergence is concentrated (see arrow placements on the $\langle \bar{\theta}_l \rangle$ profile of Figure 7 taken from Figure 4) was located almost entirely within the capping inversion layer ($r \approx 1$). Hence, only a slight amount of radiative cooling appeared within the upper mixed layer to enhance the buoyancy flux there, as perhaps manifested by the slight negative jog in the $\langle \overline{w\theta_l} \rangle$ profile between 1075 and 1125 m. Thus, in reference to assumption (f), Case 6 tends to support Lilly's original implicit assumption that the cloud-top radiative cooling

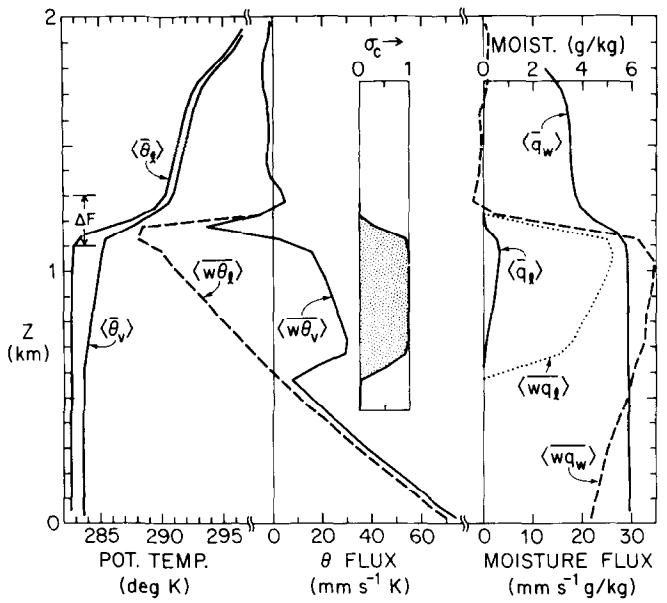

Fig. 7. Vertical profiles of mean liquid-water potential temperature and its vertical flux, virtual potential temperature and its vertical flux, cloud fraction, total specific moisture and its vertical flux, and specific liquid-water content and its vertical flux, for Case 6. Layer of strong cloud-top radiative cooling indicated by arrows at left.

occurs within the capping inversion and not within the upper mixed layer (when these regions are defined from Reynolds averaged quantities). This conclusion is also supported by the location of the cloud-top height relative to the location of the capping inversion (see Figure 7); however, it is dependent upon the model assumption that the layer of strong radiative flux divergence is locally only 50 m thick.

Unfortunately, there are some peculiarities disclosed by the radiative flux curves of Figure 4, as deduced from (14), which add uncertainty to the foregoing conclusion. One is that the layer of strong cloud-top cooling extended 50–100 m above the height where significant cloudiness was located. Only about half of this discrepancy can be explained by the smearing tendency of the second-order finite-difference technique which, in the $\bar{\theta}_l$ rate equation for example, represents $\bar{w}\bar{\theta}_l(z+\frac{1}{2}\Delta z)$ by $\frac{1}{4}[\bar{w}(z)+\bar{w}(z+\Delta z)][\bar{\theta}_l(z)+\bar{\theta}_l(z+\Delta z)]$. A second discrepancy is that the magnitude of the jump in F across the cloud-top layer is about 40% too large in Cases 6 and 7, in comparison with the value (75 mm s^{-1} C) corresponding to the cooling rate (1.5×10^{-3} K s^{-1} over one 50 m vertical grid increment) utilized in (4) in the numerical program. The computer code has been re-checked many times for an error that would explain this discrepancy, without success. For purposes of estimating an effective value of the cloud-top jump in F, Figure 4 will be used. The discrepancy is much smaller and of the opposite sign for the two dry-cloud cases. A third discrepancy is the gradual increase with height of the effective irradiance, F, below and above the cloud-top region where no radiative cooling was applied, for Cases 3,

6, and 7. For Cases 1 and 2 only, a parameterized clear-air radiative warming (or cooling) rate described in Deardorff (1974a) was utilized in addition to the cloud-top cooling of Case 2, yielding a typical value in the mixed layer of 1 K day^{-1} (warming) and above the mixed layer, -1 K day^{-1}, approximately. Within the mixed layer of Case 2, this radiative warming overcame the unexplained tendency for F to increase with height. Because of these discrepancies, results concerning the influence of cloud-top cooling cannot be stated as forcefully as would be desirable.

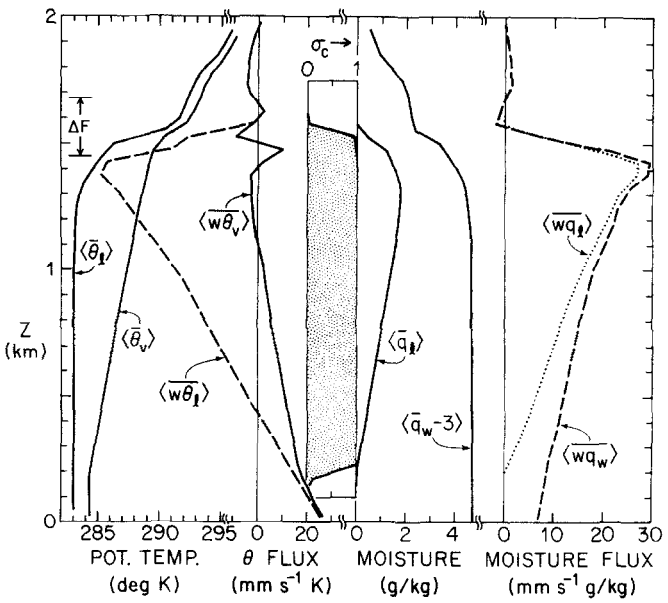

Fig. 8. Vertical profiles of mean liquid-water potential temperature and its vertical flux, virtual potential temperature and its vertical flux, cloud fraction, total specific moisture content and its vertical flux, and specific liquid-water content and its vertical flux, for Case 7, the deep stratocumulus. Note that 3×10^{-3} is subtracted from $\langle\bar{q}_w\rangle$.

The vertical profiles for Case 7 are shown in Figure 8. The effect of the deeper cloud layer is to increase substantially the liquid water content in the upper cloud layer. This appears to have caused the cloud top to be centred in the upper part of the capping inversion in this case, as opposed to the lower part in Case 6. In Case 7 the capping inversion is 50 to 100 m thicker than in Case 6, judging from the profiles of $\langle\bar{\theta}_l\rangle$ and $\langle\bar{q}_w\rangle$, but it is not clear whether this feature also is a result of the greater liquid-water content.

The rather large liquid-water content near cloud top would be expected, in reality, to cause some drizzle or light rain. Since that would in turn invalidate several other assumptions, this possibility is not treated here.

As in the previous case, the cloud-top radiative cooling in Case 7 occurred almost entirely within the capping inversion, thus promoting entrainment through cooling of

the cloud hummocks and lowering $\langle\bar{\theta}_l\rangle$ in the inversion layer rather than by contributing to enhanced buoyancy flux and turbulence in the upper well-mixed layer. Earlier, it had been concluded (Deardorff, 1976c) that about 30% of the cloud-top cooling occurred in the upper mixed layer ($r = 0.7$), but this conclusion now appears to have been an incorrect inference triggered by sampling error.

The erratic return of $\langle\overline{w\theta_l}\rangle$ toward zero in the capping inversion in Case 7, between heights of 1475 and 1525 m, may be due in part to the positive radiative flux jump in this vicinity; it may be due in part also to sampling error. It causes the profile of $\langle\overline{w\theta_v}\rangle$ to be erratic in the same layer, since $\langle\overline{w\theta_v}\rangle$ is the difference between the two large quantities: $-A\langle\overline{w\theta_l}\rangle$ and $B\langle\bar{\theta}\,\overline{wq_w}\rangle$ (see (7d)). This feature raises the possibility that in actual stratocumulus capping inversions, the detailed shape of the ensemble-averaged buoyancy flux profile is not simple or universal, but may depend upon the distribution of radiative flux and perhaps also the cloud water content.

With considerable certainty, the numerical results from Cases 4, 6 and 7 do indicate that the most negative buoyancy flux of entrainment lies somewhere within the capping inversion where σ_c decreases from 1 to 0. Assumption (c) is thus not confirmed.

For Case 7, the initial soil moisture had been increased to a value close to the saturated-soil value (see Table I) in an attempt to hold the cloud base close to the ground. However, the evaporation rate was not large, due to the high humidity of the air near the ground and the weak solar radiation received there, and the moisture flux near the top of the mixed layer again exceeded that at the surface. Hence, cloud base rose some 20 m during the analysis period of Case 7, and even more during the earlier, settling-down part of the integration, due to the consequent drying of the mixed layer as a whole. Also, as has been seen with Figures 5 and 7, increased evaporation leads to increased cloud buoyancy, greater entrainment, and greater moisture flux in the entrainment layer. The ease with which the moisture flux of entrainment exceeds the evapotranspiration rate at the surface appears responsible for the rarity of stratocumulus cloud base being at the surface (fog) for moderately deep mixed layers of the type modeled here. The condition for which fog of this type should be less unlikely is that of the shallow mixed layer (of order only a few hundred meters) with a capping inversion that is consequently also thin (of order 30 m). Then the upper-cloud radiative cooling is less confined to the capping inversion but extends relatively farther down into the mixed layer. The latter, being shallow, then cools more rapidly. The cooling tendency could then overcome the entrainment-flux drying tendency to promote a lowering of cloud base to the surface. This behavior was observed by Oliver *et al.*, (1978) using a one-dimensional model.

5. Turbulence Energy and its Budget

Profiles of the vertical and horizontal portions of the total turbulence energy for Cases 1–7 are shown in Figures 9 and 10, respectively. The abscissa has been scaled

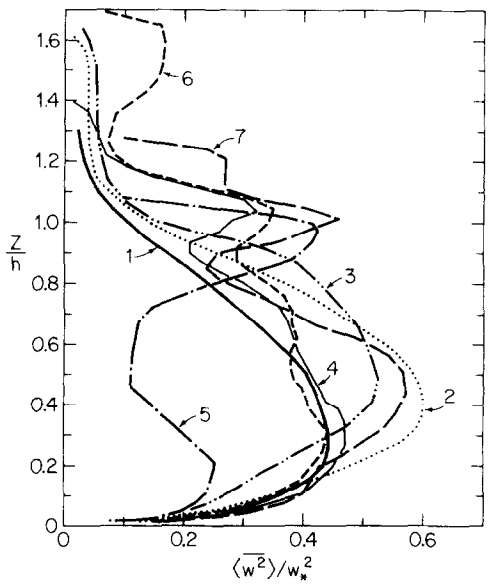

Fig. 9. Vertical profiles of the variance of vertical velocity normalized by values of generalized w_*^2 for Cases 1–7 indicated by numerals.

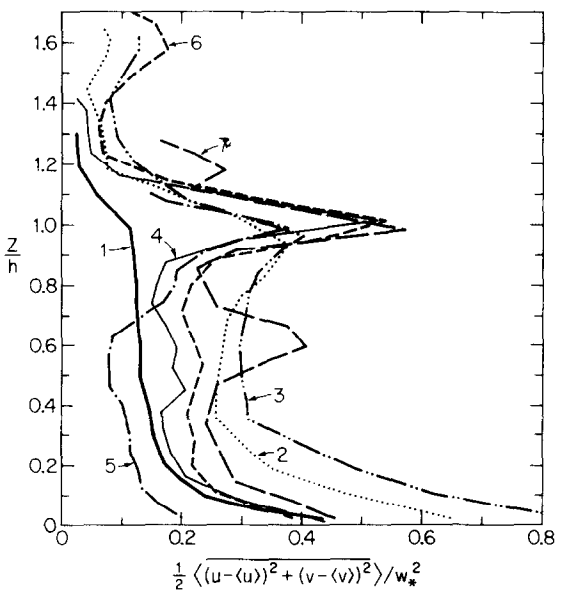

Fig. 10. Vertical profiles of the horizontal turbulence intensity, normalized by w_*^2, for Cases 1–7.

by the square of a generalized convective velocity scale, w_*, defined by

$$w_*^3 = 2.5 \frac{g}{\theta} \int_0^{h_2} \langle w\theta_v \rangle \, dz \tag{17}$$

where h_2 is the height from the surface to the top of the capping inversion, or just above the region of negative buoyancy flux of entrainment. The ordinate, z, has been scaled by the values of h listed in Table I. The factor 2.5 in (17) allows this definition of w_* to become approximately synonomous with the usual definition of the convective velocity scale for the clear mixed layer (see Deardorff, 1970). Values of w_* for the 7 cases and others to be mentioned later are listed in Table II.

TABLE II

Derived quantities

Case	w_* (ms^{-1})	w_e (mm s^{-1}) observed directly	w_e (mm s^{-1}) from (15a,b)	w_e/w_* (average)	β	$\Delta\theta_v$ (C)	$\Delta\theta_e$ (C)	Ri_*	r'	Ri_σ	$\sigma_w(h)$ (m s^{-1})	$\sigma_w(h)/w_*$
1	2.01	30	24	0.0134	0.38	1.8	−2.6	20	0.045	192	0.65	0.32
2	1.81	–	–	–	0.28	2.1(?)	(−2.8)	–	0.011	–	0.70	0.39
3	1.44	–	–	–	0.24	1.5(?)	(−4.4)	–	0.024	–	0.58	0.40
4	1.46	5.9	6.4	0.0042	1.06	7.7	3.0	172	0.088	610	0.77	0.53
5	1.50	158	–*	0.105	–**	2.4	−2.6	65	–**	66††	1.00	0.67
6	1.39	23	18	0.0147	0.85	5.7	2.0	116	0.044	350	0.80	0.58
7	0.98	21	19	0.020	1.06	2.9	1.9	159	0.088	350	0.66	0.67
W2	1.92	11	12	0.0060	0.18	2.2	−3.6	29	0.023	270	0.63	0.33
S1	0.012	0.28	(.18)†	0.023	0.21	1.5	–	13	0.036	187	0.0035	0.29
S2	0.012	0.16	(.05)†	0.013	0.12	2.6	–	23	0.015	420	0.0031	0.26
4.4	1.55	36	–*	0.023	0.49	5.5	2.2	108	0.031	340	0.88	0.57
4.5	1.40	32	–*	0.023	0.53	3.8	0.0	93	0.091	360	0.72	0.51
4.6	1.24	24	–*	0.019	0.70	2.9	−0.7	93	0.060	330	0.66	0.53
4.7	1.27	46	–*	0.036	0.65	2.2	−1.2	68	0.048	116††	0.67	0.53
4.8	1.20	73	–*	0.061	–**	2.0	−1.6	72	–**	93††	0.74	0.62
4.9	1.28	99	–*	0.077	–**	1.5	−1.9	50	–**	57††	0.87	0.68

Notes:

* Lack of ensemble average precluded a reliable estimate.

** Region of negative buoyancy flux near cloud top was absent or uncertain due to cloud top entrainment instability.

† Estimate was from $-\langle wT \rangle_h / \Delta T$ with $\langle wT \rangle_h$ being obtained from upward extrapolation of profile in lower and middle mixed layer. Result considered less accurate than direct method.

†† $(h - h_b)$ was utilized in place of h in the definition of Ri_σ.

Except for Case 5, Figure 9 indicates that the w_* scaling for cloud and dry-cloud cases is still useful but tends to yield somewhat greater values of $\langle \overline{w^2}/w_*^2 \rangle$ than in the clear mixed layer. The profile for Case 3 discloses significantly greater variance in the upper mixed layer than in the lower mixed layer, due to buoyant energy input being mainly in the upper portion in this case of near zero surface buoyancy flux.

Cases 4–7 exhibit a strong secondary maximum in $\langle \overline{w^2} \rangle$ between 0.9 and 1.1 or 1.2 z/h. This is missing in the cases lacking representation of cloud water. Much of this feature (above $z/h = 1$) cannot be trusted as real, and appears to be a result of truncation errors and aliasing of internal-wave motions within the strong capping inversions of Cases 4, 6 and 7. However, a peak in $\langle w^2 \rangle$ just below $z = h$ appears in the aircraft measurements of Coulman (1978). The total noise in $\bar{w}$ above $z = h$ in Case 6 is readily apparent in Figure 11c, which shows calculated fields of the velocity components at particular times in an x–z plane ($y = 5\Delta y$). Examples from Cases 2 and 5 are also shown in Figure 11; in Case 2 the effects of truncation error near $z = h$

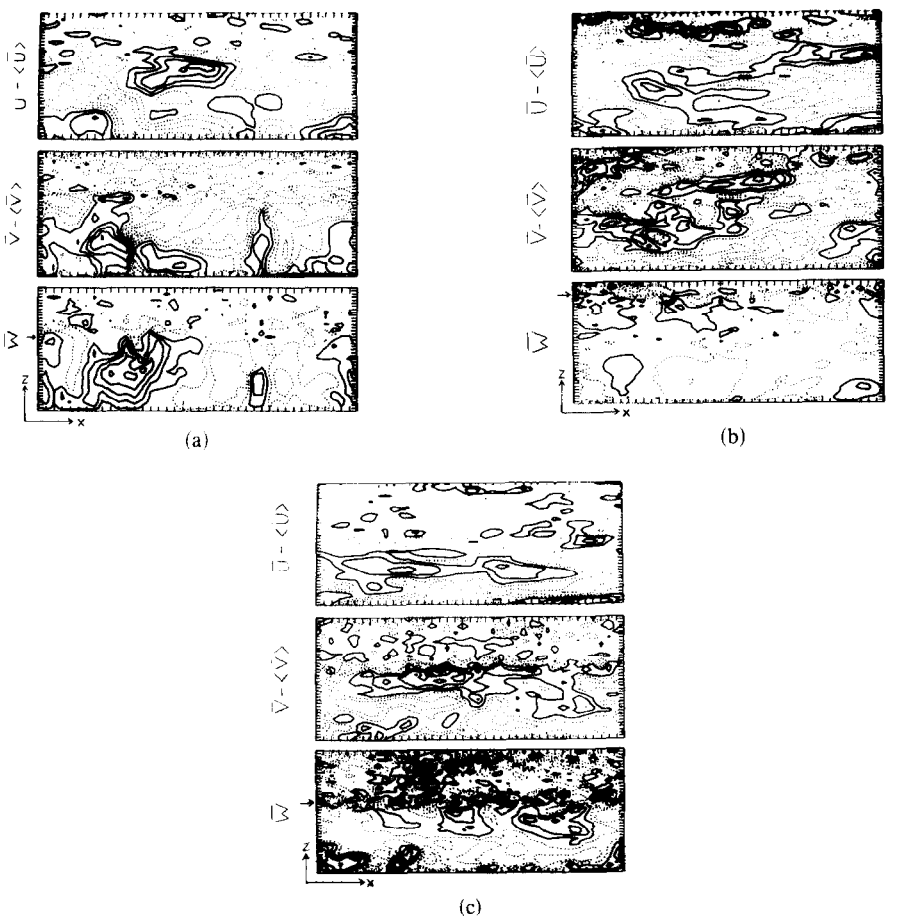

Fig. 11. Vertical cross-sections of resolvable-scale west-east wind eddies (upper third), south-north wind eddies (middle third), and vertical velocity (lower third) occurring at a particular time within a particular x–z plane. Solid contours denote positive values, dotted contours denote negative values. Zero contour lies midway between adjacent solid and dotted contours. Tick marks denote grid intervals. Horizontal scale is exaggerated by a factor of 2.5 relative to vertical scale. (a top left): Case 2. Contour interval for $\bar{u}$ is 0.58 m s^{-1}, for $\bar{v}$ is 0.44 m s^{-1}, and for $\bar{w}$ is 0.82 m s^{-1}; (b top right): Case 5. Contour interval for $\bar{u}$ and $\bar{v}$ is 0.31 m s^{-1}, and for $\bar{w}$ is 0.91 m s^{-1}; (c center): Case 6. Contour interval for $\bar{u}$ is 0.42 m s^{-1}, for $\bar{v}$ is 0.37 m s^{-1}, and for $\bar{w}$ is 0.46 m s^{-1}.

do not appear to be serious, perhaps because the capping inversion was not sharp. The same may be said for Case 5, for which the capping inversion was also weak. In addition, in this latter case the cloud-top evaporative cooling extended much farther down into the cloud, due to the entrainment instability. Thus, there was improved vertical resolution in the zone where evaporative cooling contributes to buoyant instability and vertical motions. The pronounced maximum in $\langle \overline{w^2} \rangle$ in this case, centered just below $z = h$, is therefore considered to be realistic.

Because the secondary maxima in Cases 4, 6 and 7 resemble the maximum of Case 5, and because they occur only in the liquid-water cloud simulations, it is here postulated that even in these cases the secondary maximum in $\langle \overline{w^2} \rangle$ has a basis in reality. The physical mechanism is, again, the evaporative cooling of descending, entraining air in the region $0.95 < z/h < \sim 1.05$ where the cloud fraction lies between 1 and 0. Even when this process is not strong enough to produce cloud-top entrainment instability, it acts towards increasing $\langle w\theta_v \rangle$ from the value it would otherwise have in the absence of cloud liquid water.

An interesting feature shown by Figure 11 is a strong tendency for the vertical motions or eddies in the cloud layer to be distinct from those in the subcloud layer. Comparing Figure 11(b) with Figure 11(a) for the dry cloud or with a similar eddy depiction for Case 1 from Deardorff (1974b, Figure 2), one sees that when a substantial stratocumulus layer is present, the $\bar{w}$ eddies do not so often extend from the surface to the top of the mixed layer. This tendency would have been enhanced had the model admitted weak radiative warming near cloud base. Figure 11 also shows, as expected, much larger horizontal scales for the $\bar{u}$ and $\bar{v}$ components than for the $\bar{w}$ component.

The profiles of $\frac{1}{2}\langle \overline{(u - \langle u \rangle)^2} + \overline{(v - \langle v \rangle)^2} \rangle / w_*^2$ in Figure 10 disclose a strong maximum near $z = h$ associated with small changes in mean velocity across the capping inversion in Cases 2–7, of magnitude near 1 m s^{-1}. (In Case 1 the velocity differential across Δh was even smaller, and no distinct maximum is discernible.) Only about 4% of the velocity variance at these peaks was associated with subgrid scale motions. As was the case with $\langle \overline{w^2} \rangle$, the horizontal turbulence energy when scaled by w_*^2 is calculated to be greater by a factor of up to 2 for cases with energy production mechanisms in the mid and upper mixed layer than for the case of the clear mixed layer.

5.1 Turbulence energy budget

Terms in the budget equation for the total turbulence energy, $\mathscr{E}$, for Case 6 are displayed as functions of height in Figure 12. Except for the dissipation rate, ε, positive values as plotted contribute towards growth of $\langle \mathscr{E} \rangle = \frac{1}{2}\langle \bar{u}''^2 + \bar{v}''^2 + \bar{w}^2 \rangle + \langle \bar{E} \rangle$, and negative values towards decay. The turbulence redistribution terms shown are just the resolvable portions; for energy transport: $-\frac{1}{2}\partial\langle \bar{w}(\bar{u}''^2 + v''^2 + \bar{w}^2) \rangle / \partial z$, and for pressure transport: $-\partial\langle \overline{wp''}/\rho_0 \rangle / \partial z$. Presumably, the subgrid-scale portions of these terms are of minor importance except in the lowest 50 m and in and above the capping inversion. In the latter region there is a very large residual imbalance which,

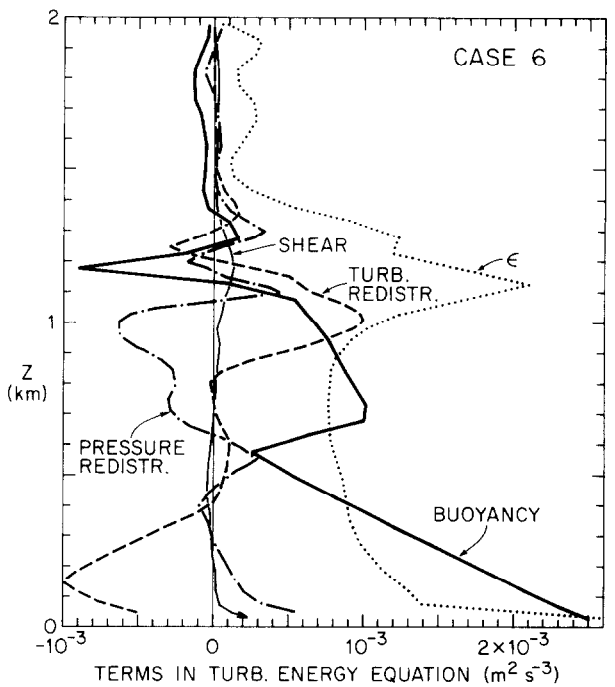

Fig. 12. Vertical profiles of terms in the turbulence kinetic energy equation for Case 6. Positive values indicate sources, negative values sinks, except for the rate of dissipation, ε. The turbulence redistribution term (dashed) and pressure redistribution term (dash-dot) do not include the subgrid-scale contribution. The imbalance at and above the mixed-layer top reflects truncation errors as well as the subgrid-scale contribution to the two curves mentioned.

however, is probably mostly attributable to truncation errors rather than to the subgrid-scale redistribution terms or to the time rate of change of $\langle \mathscr{E} \rangle$. In particular, terms that could be formulated from (1) to represent loss of resolvable-scale turbulence energy to subgrid-scale turbulence, $(\bar{E})$, would in effect be discretized differently and less compactly than were the corresponding stress-strain terms representing the main source of $\bar{E}$. Also, in formulating the model outputs, the buoyancy variable and cloud saturation were determined at the pressure grid points, after vertical averaging, rather than at the $\bar{w}$ grid points as in the numerical integrations. For these reasons, truncation errors were potentially large.

In the region where the budget is most trustworthy, an interesting feature emerges, however. As expected from previous studies, the pressure redistribution term tends to offset one-third to one-half of the turbulence redistribution term. However, at and just below cloud base the two terms act in concert, with the pressure-redistribution term being the larger in maintaining turbulence energy in this region where the buoyancy force becomes small.

Vertical profiles of the resolvable-scale vertical transports of turbulence energy (and its horizontal components alone), and of pressure fluctuations, are shown in

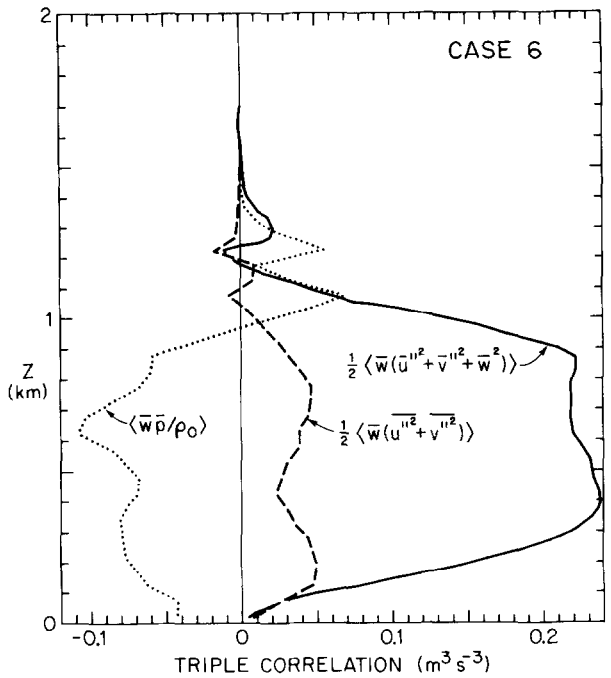

Fig. 13. Vertical profiles of resolvable scale triple-correlation terms of Case 6. The negative of the vertical derivative of the kinetic energy transport term (solid curve) is the 'turbulence redistribution' term of Figure 12; the negative of the vertical derivative of the pressure transport term (dotted curve) is the 'pressure redistribution' curve of Figure 12.

Figure 13. If normalized by w_*^3, the transport of turbulence energy will be seen to have a peak value about 20% smaller than found for the clear mixed layer by Willis and Deardorff (1974), but with a maximum that is much broader in the vertical. Roughly 80% of the vertical transport of turbulence energy is seen to be associated with the transport of $\frac{1}{2}\bar{w}^2$.

The shear-stress production term:

$$\langle\overline{uw}\rangle\frac{\partial\langle\bar{u}\rangle}{\partial z}-\langle\overline{vw}\rangle\frac{\partial\langle\bar{v}\rangle}{\partial z}$$

is seen to have been rather unimportant except in the lowest 50 m and perhaps in the capping inversion, where, however, the imbalance dominates. Across the capping inversion there was a mean shear of about 1 m s^{-1} per 150 m in magnitude existing in both $\langle\bar{u}\rangle$ and $\langle\bar{v}\rangle$. Although the shear production appears to have been small in the capping inversion in comparison to the buoyant destruction of energy, and assumption (d) appears to have been fulfilled, this might not have been true had velocity jumps of several meters per second occurred.

The imbalance of terms and absence of a strong source to maintain $\langle\overline{w^2}\rangle$ against dissipation at and above $z = 1.05$ h support the earlier conclusion that the secondary

maxima in $\langle \overline{w^2} \rangle$ calculated for this region in Cases 4, 6 and 7 were grossly distorted from truncation errors.

6. The Entrainment Rate

It might be thought that a numerical model with 50 m mesh could not begin to resolve the entrainment process. To estimate what fraction of the calculated entrainment occurred on scales resolved by the model and what fraction occurred on the subgrid scale, we may turn to Lilly's type of entrainment-flux relation:

$$w_e = -\frac{\langle \overline{w\theta_l} \rangle_h}{\Delta\theta_l} + \frac{(F_2 - F_h)}{\Delta\theta_l} = -\frac{\langle \bar{w}\bar{\theta}_l \rangle_h}{\Delta\theta_l} + \frac{(F_2 - F_h)}{\Delta\theta_l} - \frac{\langle \overline{w'\theta_l'} \rangle_h}{\Delta\theta_l} \tag{18a}$$

$$w_e = -\frac{\langle \overline{wq_w} \rangle_h}{\Delta q_w} = -\frac{\langle \bar{w}\bar{q}_w \rangle_h}{\Delta q_w} - \frac{\langle \overline{w'q_w'} \rangle_h}{\Delta q_w} \tag{18b}$$

and identify the last term on the right in (18a,b) as the subgrid-scale contribution. Here, h is the height of the base of the capping inversion (about at the top of the nearly linear section of the mixed-layer conservative flux profiles), and h_2 is the height of the top of the capping inversion. Results indicate that the subgrid-scale contributions ranged from 7 to 21% of the total entrainment rate deduced from (18), which are surprisingly small percentages. (Of course, the ultimate mixing which accomplishes saturation on the microscale is associated with scales of motion down to about a centimeter.) This result encourages an analysis of the numerically calculated entrainment rates, even though the subgrid-scale contribution to entrainment may have been erroneously small.

Both the average of (15a) and (15b) and a more direct method were used to estimate the entrainment rate, w_e. The direct method in Cases 4–7 was to identify the height near cloud top at which 50% cloud cover occurred, and measure its average rate of increase over the time period analyzed. In case 1 and other non-cloud cases, the direct method utilized the height of most negative buoyancy flux instead. In Cases 2 and 3, w_e was not estimated because of distortions in shape of the interfacial layer caused by the enforced placement of radiative cooling at a fixed height. Resulting values of w_e are listed in Table II. Other cases listed there are: W2: the clear-sky Wangara boundary-layer simulation of Deardorff (1974a) 2.8 hours later in the day than case 1; S1 and S2: the laboratory convective mixed-layer experiments of Willis and Deardorff (1974); and cases 4.4 to 4.9: cases akin to and immediately preceeding Case 5 reported by Deardorff (1980).

Theories on entrainment usually require knowledge or assumptions about the buoyancy flux in the entrainment zone. The ratio

$$\beta = -h\langle \overline{w\theta_v} \rangle_1 \Big/ \int_0^{h_2} \langle \overline{w\theta_v} \rangle \, \mathrm{d}z$$

is therefore also listed in Table II, where subscript 1 refers to the height of the most negative value of the entrainment buoyancy flux. The value $\beta = 0.5$ recommended by Deardorff (1976a) is a fair average of the numerically derived values, but the scatter is much too great to permit tangible conclusions. In estimating β, the most negative value of $\langle \overline{w\theta_v} \rangle$ that actually occurred was used, rather than a linearly extrapolated value following a zero-order jump model. Had the latter been used, β values would be nearly doubled in Cases 1, W2, S1 and S2.

The ratio β is expected to decrease with increasing interfacial stability (Zeman and Tennekes, 1977), one measure of which (e.g., see Turner, 1968, or Kato and Phillips, 1969) is an overall buoyancy Richardson number, Ri_*, defined by

$$\mathrm{Ri}_* = \frac{g}{\theta_0} h \Delta\theta_v / w_*^2 \tag{19}$$

where $\Delta\theta_v$ is the jump in $\langle \theta_v \rangle$ across the capping inversion; $\Delta\theta_v$ and Ri_* are also listed in Table II. If β is plotted against Ri_*, however, no reliable trend is apparent.

The 'area' ratio

$$r' = -\int_0^{h_2} \langle w\theta_v \rangle_{\mathrm{neg}} \, \mathrm{d}z \Big/ \int_0^{h_2} \langle w\theta_v \rangle_{\mathrm{pos}} \, \mathrm{d}z$$

recommended by Kraus and Schaller (1978b) as a closure assumption is also listed in Table II. The variability of this ratio is also much too large to permit tangible conclusions, other than to say its order of magnitude is $r' \sim 0.05$. Again, no detectable trend of this ratio with Ri_* is apparent from the tabulated data. The negative-flux area $\sim \Delta h \langle w\theta_v \rangle_1$, where Δh is the thickness of the entrainment zone with negative buoyancy flux which is roughly equal to the thickness of the capping inversion. For a case having a moderately small value of Δh but large values of positive buoyancy flux in the mixed layer, the closure assumption $r' = \text{const}$ may require a very large negative value for $\langle w\theta_v \rangle_1$ (e.g., see Figure 2). However, the latter quantity is bounded in magnitude by the product of the standard deviations of w and θ_v at $z = h_1$. Hence, the area closure assumption does not seem sufficiently general to handle cases with cloud buoyancy and radiative cooling inside the upper mixed layer, although it is well suited to the clear mixed layer.

These results for β and r' suggest that $\langle w\theta_v \rangle$ in the capping inversion is influenced considerably by factors other than the entrainment rate, such as magnitude and vertical distribution of radiative cooling, cloud water content, and capping-inversion thickness relative to h. It seems therefore not to be a sufficiently fundamental quantity on which to base an entrainment closure assumption when stratocumulus is present.† Furthermore, its most negative value of entrainment occurs at a height intercepting cloud domes where the air is not all saturated, in violation of assumption (c); correcting this assumption would complicate the proper implementation of a

† *Note added in proof*: However, a new interpretation by S. A. Stage (Ph.D. dissertation, 1979, Department of Atmospheric Sciences, University of Washington, Seattle, Washington 98195), which distributes the entrainment fluxes between the surface and $z = h$ and uses a closure based on the vertical integral of the distributed buoyancy flux of entrainment, is very promising.

closure assumption based upon β or r'. If the foregoing proves to be true, a more fundamental and convenient closure assumption for the entrainment rate that could be used or tested is of the type introduced by Turner (1968); namely,

$$w_e/w_* = F'(\mathrm{Ri}_*)$$

where F' is a function to be determined. A plot of w_e/w_* versus Ri_* is given by Figure 14. This plot is fairly successful in separating the data into clear-sky and cloud-capped mixed-layer cases, through which the two curves have been faired by eye.

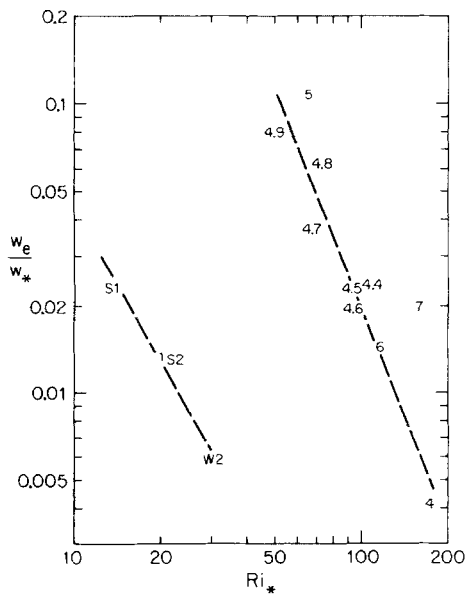

Fig. 14. The entrainment rate w_e, normalized by w_*, as a function of the w_*-based overall Richardson number, Ri_* for Cases 1, 4–7. Also listed are results for Cases W2, S1, S2, and 4.4–4.9.

A dual plot of the nature of Figure 14 does not solve the problem, however, of how to treat entrainment when the mixed-layer cloud deck is thin or broken, since w_e/w_* is calculated to be about 30 times greater, at a given value of Ri_*, for the cloud-capped than for the clear cases. Now, presumably it is the vertical turbulence intensity at $z = h$ that promotes the entrainment, and it was seen that $\langle \overline{w^2} \rangle$ there was considerably greater in the cloud-capped mixed layers modeled. This finding suggests that $w_e/\sigma_w(h)$ be tested as a function of

$$\mathrm{Ri}_\sigma = \frac{g}{\theta_0} \Delta\theta_v h/\sigma_w^2(h) \tag{20}$$

where $\sigma_w(h)$ is the standard deviation of w at $z = h$. Values of Ri_σ and $\sigma_w(h)$ are also listed in Table II. This plot appears as Figure 15, for which two modifications were made that apply to some of the cases. First, in Cases 4.7–4.9 and Case 5 of very rapid entrainment, the fluxes of semi-conservative properties were non-linear in the mixed

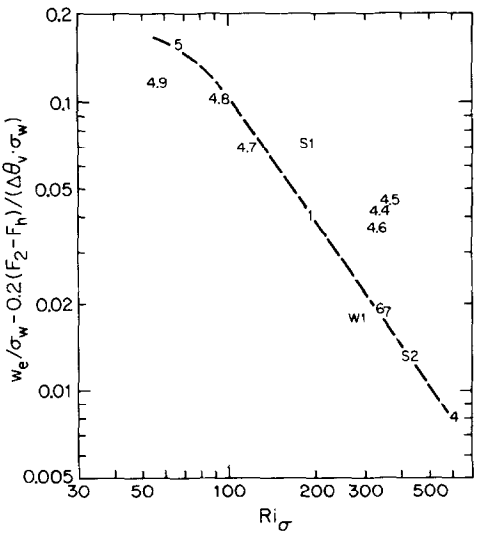

Fig. 15. The entrainment rate normalized by σ_w at $z = h$, as a function of Ri_σ for the same cases as in Figure 14. The ordinate excludes the estimated influence of indirect entrainment associated with radiative cooling of the capping inversion in Cases 6 and 7.

layer, and tended to have one slope in the cloud layer and a different one in the sub-cloud layer. The length scale h appearing in Ri_σ was accordingly replaced by the cloud thickness in those 4 cases. Second, in Cases 6 and 7 radiative cooling in the capping inversion was presumably enhancing the entrainment rate. A measure of this effect was incorporated by utilizing as ordinate the quantity

$$w_e/\sigma_w - 0.2(F_2 - F_h)/(\sigma_w \Delta\theta_v)$$

in place of w_e/σ_w. The form of the subtracted quantity is suggested from dimensional considerations and from McEwen and Paltridge (1976) although they utilized unity for the constant of proportionality. Here, a multiplying constant greater than 0.54 would drive w_e/σ_w negative in Case 7. (It might be thought that (18a) would indicate that the subtracted term in the ordinate should contain $\Delta\theta_l$ instead of $\Delta\theta_v$, along with a multiplying factor of unity. However, this argument implies that in a given situation, $\langle w\theta_l\rangle_h$ is independent of $F_2 - F_h$. Equation (18b) contradicts this possibility; i.e., if (18a) says that w_e increases when $(F_2 - F_h)/\Delta\theta_l$ increases, (18b) says that w_e would remain unchanged. Moreover, in place of (18a) one could utilize an equation involving θ_e instead of θ_l, showing that θ_l is used in (18a) only as a matter of convenience.) The influence of any radiative cooling deposited within the upper well-mixed layer is taken into account implicitly through the resulting enhancement of $\langle w\theta_v\rangle$ and of $\sigma_w(h)$.

Figure 15 collapses the entrainment data points as well or better than is to be expected considering uncertainties associated with truncation errors in the capping inversion. To a considerable extent, the use of σ_w in place of w_* to scale w_e probably removes some of the associated error, since if σ_w was spuriously large at $z = h$ in

some of the cases, so also was the calculated entrainment rate from the numerical integrations. In practice, $\sigma_w(h)$ may be unknown and may require a further model assumption. It is natural to normalize it by w_*, and values of the ratio $\sigma_w(h)/w_*$ are also listed in Table II. Its value is seen to lie near 0.33 ± 0.05 for clear-sky mixed layers and 0.59 ± 0.07 for stratocumulus-capped mixed layers, although the latter value may be too large due to truncation errors. The value of this ratio for thin or broken stratocumulus layers, the effect upon it of wind shear in the capping inversion, and the proper manner of treating the influence upon w_e of radiative cooling within the capping inversion (in a plot like Figure 15) remain topics for further research.

7. Conclusions and Recommendations

The following conclusions may be drawn from this study:

(i) Over land, the cloud buoyancy flux and entrainment rate are sensitive to the soil moisture content, holding other initial conditions the same.

(ii) The moisture flux just below the top of the stratocumulus layer typically exceeds the evaporation rate at the surface, especially when the cloud base is low. The consequent drying tendency typically exceeds any cooling tendency and prevents cloud base from growing down to the surface, for mixed layers of height of order 1.5 km or more as in this study.

(iii) Unless cloud-top entrainment instability occurs, the buoyancy flux undergoes a double jump in the vicinity of the cloud top. Negative values of entrainment lie just above positive values associated with evaporative cooling and cloud buoyancy. Thus, assumption (c) used in theoretical models (see Section 1) is not fulfilled.

(iv) Cloud-base height, as well as cloud-top height, is variable, typically over a 100 m height interval, within the context of the horizontal average or ensemble average.

(v) There is a tendency for the eddies in the cloud layer to become distinct from those in the subcloud layer, even when the stratocumulus cover is solid and the entire boundary layer appears well mixed otherwise.

(vi) Turbulence energy near cloud base, when little or no buoyant production is present there, is supplied mostly through the pressure redistribution term: $-\partial\langle wp/\rho_0\rangle/\partial z$.

(vii) The zero-order jump-model relationships at cloud-top height, (18a,b), are reasonably accurate for the purpose of estimating the entrainment rate, even though the capping inversion is of substantial thickness in violation of assumption (b) used in their derivation.

(viii) The normalized entrainment rate, $w_e/\sigma_w(h)$, appears to be very usefully dependent upon the overall buoyancy Richardson number, Ri_σ (which is also based

upon $\sigma_w(h)$) if the influence of indirect entrainment caused by radiative cooling in the capping inversion is allowed for; see Figure 15.

The final four conclusions are more tentative:

(ix) If cloud-top radiative cooling extends over only about 50 m or less, most or nearly all of it occurs within the capping inversion of deep or moderately deep mixed layers. If it extends over 100 m, as estimated by Businger and Kahn (1979), a substantial fraction of it probably lies within the upper mixed layer.

(x) The buoyancy flux $\langle w\theta_v \rangle$ within the capping inversion does not appear to be uniquely related to the buoyancy flux at lower heights, nor does the integral of the first appear to be closely related to the integral of the second, except for the clear-sky mixed layer.

(xi) Evaporative cooling of entraining air enhances σ_w within the capping inversion, even though it may not be so strong as to produce cloud-top entrainment instability. The ratio $\sigma_w(h)/w_*$ is found to have a value near 0.33 for clear-sky mixed layers and near 0.59 for cloud-capped mixed layers, though the latter value is thought to be somewhat inflated from truncation errors in the numerical calculations.

(xii) Indirect entrainment associated with radiative cooling of the cloud air within the capping inversion proceeds at a much lesser rate than $(F_2 - F_h)/\Delta\theta_v$, where $F_2 - F_h$ is the kinematic radiative flux difference across the capping inversion. A proportionality constant of order 0.2 is suggested by the numerical results.

In future three-dimensional studies of cloud-capped mixed layers, more resolving power is needed, especially within the capping inversion. A vertical grid increment of 10–15 m instead of 50 m in this region would greatly reduce truncation errors, would allow more accurate estimates of entrainment rate and negative buoyancy flux, and would allow more accurate placement, locally, of cloud-top radiative cooling. The latter should be allowed to depend on cloud-water content at and above a given grid volume. The use of a subgrid-scale cloud-fraction parameterization would probably be worthwhile, especially near cloud top.

The present criterion for subgrid-scale turbulence to vanish when the local Richardson number exceeds a critical value of 0.23 seems to have been too stringent. It seems to have caused insufficient subgrid-scale turbulence energy to exist in and above the capping inversion, and, therefore, insufficient physical damping of resolvable motions and internal waves. The persistence of excessive noise on the computational grid above the mixed layer was probably associated more with this deficiency than with spurious reflection of wave energy from the upper boundary of the computational domain. A recent study by Findikakis and Street (1979) finds that the subgrid-scale motions do not quench, but persist weakly for large Richardson numbers when larger scale stretching motions occur. The subgrid-scale parameterization of Sommeria (1976) qualitatively accomplishes this result.

Mesoscale variability, especially in the large-scale vertical velocity, is an important part of actual stratocumulus-capped mixed layers. This variability can cause cloud-free patches or patterns on the 10–15 km scale, but cannot yet be modeled if the main elements of the convective turbulence are also to be modeled explicitly. However, results from an improved three-dimensional model on the boundary-layer scale might be parameterized for use within a mesoscale model.

Acknowledgments

This study was made possible by financial support from Grant ATM-77-24559 of the Global Atmospheric Research Program, Climate Dynamics Research Section, of the U.S. National Science Foundation. Numerical calculations were performed on the CDC 7600 computer of the National Center for Atmospheric Research while the writer was affiliated there. Thanks are due to Ed Tollerud for much data reduction and analysis, and to Brenda Mobley for assistance. The author gratefully acknowledges stimulating inputs from Drs D. Lilly, J. Businger, D. Randall, L. Mahrt and W. Schubert during the course of this study.

References

Albrecht, B. A., Betts, A. K., Schubert, W. H., and Cox, S. K.: 1979, 'A Model of the Thermodynamic Structure of the Trade-Wind Boundary Layer: Part I. Theoretical Formulation and Sensitivity Tests', *J. Atmos. Sci.* **36**, 73–89.

André, J. C., De Moor, G., Lacarrère, P., and du Vachat, R.: 1976, 'Turbulence Approximation for Inhomogeneous Flows: Part II. The Numerical Simulation of a Penetrative Convection Experiment', *J. Atmos. Sci.* **33**, 482–491.

Arakawa, A.: 1966, 'Computational Design for Long-Term Numerical Integration of the Equations of Fluid Motion: Two-dimensional Incompressible Flow, Part I', *J. Comp. Phys.* **1**, 119–143.

Ball, F. K.: 1960, 'Control of Inversion Height by Surface Heating', *Quart. J. Roy. Meteorol. Soc.* **86**, 483–494.

Betts, A. K.: 1973, 'Non-precipitating Cumulus Convection and its Parameterization', *Quart. J. Roy. Meteorol. Soc.* **99**, 178–196.

Businger, J. A., Wyngaard, J. C., Izumi, Y., and Bradley, E. F.: 1971, 'Flux-Profile Relationships in the Atmospheric Surface Layer', *J. Atmos. Sci.* **28**, 181–189.

Clarke, R. H., Dyer, A. J., Brook, R. R., Reid, D. G., and Troup, A. J.: 1971, 'The Wangara Experiment: Boundary Layer Data', CSIRO Div. of Meteorol. Phys. Tech. Paper No. 19, 340 pp.

Coulman, C. E.: 1978, 'Convection in Stratiform Cloud', *J. Rech. Atmos.* **12**, 21–33.

Deardorff, J. W.: 'Convective Velocity and Temperature Scales for the Unstable Planetary Boundary Layer', *J. Atmos. Sci.* **27**, 1211–1213.

Deardorff, J. W.: 'Three-Dimensional Numerical Study of the Height and Mean Structure of a Heated Planetary Boundary Layer', *Boundary-Layer Meteorol.* **7**, 81–106.

Deardorff, J. W.: 1974b, 'Three-Dimensional Numerical Study of Turbulence in an Entraining Mixed Layer', *Boundary-Layer Meteorol.* **7**, 199–226.

Deardorff, J. W.: 1976a, 'On the Entrainment Rate of a Stratocumulus-Topped Mixed Layer', *Quart. J. Roy. Meteorol. Soc.* **102**, 563–582.

Deardorff, J. W.: 1976b, 'Usefulness of Liquid-Water Potential Temperature in a Shallow-Cloud Model', *J. Appl. Meteorol.* **15**, 98–102.

Deardorff, J. W.: 1976c, 'Clear and Cloud-Capped Mixed Layers: Their Numerical Simulation, Structure and Growth and Parameterization', in *Seminars on the Treatment of the Boundary Layer in Numerical*

Weather Prediction, European Centre for Medium Range Weather Forecasts, Reading, England, 6–10 Sept. 1976, 234–284.

Deardorff, J. W.: 1980. 'Cloudtop Entrainment Instability', *J. Atmos. Sci.* **37**, 131–147.

Findikakis, A. N. and Street, R. L.: 1979, 'An Algebraic Model for Sub-grid-scale Turbulence in Stratified Flows', *J. Atmos. Sci.* **36**, 1934–1949.

Kahn, P. H. and Businger, J. A.: 1979, 'The Effect of Radiative Flux Divergence on Entrainment of a Saturated Convective Boundary Layer', *Quart. J. Roy. Meteorol. Soc.* **105**, 303–305.

Kato, H., and Phillips, O. M.: 1969, 'On the Penetration of a Turbulent Layer into Stratified Fluid', *J. Fluid Mech.* **37**, 643–655.

Kraus, H. and Schaller, E.: 1978a, 'Steady-State Characteristics of Inversions Capping a Well-Mixed Planetary Boundary Layer', *Boundary-Layer Meteorol.* **14**, 83–104.

Kraus, H. and Schaller, E.: 1978b, 'A Note on the Closure in Lilly-Type Inversion Models', *Tellus* **30**, 84–88.

Lilly, D. K.: 1975, 'On the Computational Stability of Numerical Solutions of Time-dependent Non-linear Geophysical Fluid Dynamics Problems', *Monthly Weather Rev.* **93**, 11–26.

Lilly, D. K.: 1968, 'Models of cloud-topped Mixed Layers under a Strong Inversion', *Quart. J. Roy. Meteorol. Soc.* **94**, 292–309.

Manabe, S.: 1969, 'Climate and the Ocean Circulation, I. The Atmospheric Circulation and the Hydrology of the Earth's Surface', *Monthly Weather Rev.* **97**, 739–805.

McEwan, A. D. and Paltridge, G. W.: 1976, 'Radiatively Driven Thermal Convection Bounded by an Inversion – a Laboratory Simulation of Stratus Clouds', *J. Geophys. Res.* **81**, 1095–1102.

Mellor, G. L.: 1977 'The Gaussian Cloud Model Relations', *J. Atmos. Sci.* **34**, 356–358.

Oliver, D. A., Lewellen, W. S., and Williamson, G. G.: 1978, 'The Interaction between Turbulent and Radiative Transport in the Development of Fog and Low-Level Stratus', *J. Atmos. Sci.* **35**, 301–316.

Randall, D. A.: 1979, 'On the Entraining Moist Boundary Layer, Part I. Conditional Instability of the First Kind Upside-down', submitted to *J. Atmos. Sci.*

Schubert, W. H.: 1976, 'Experiments with Lilly's Cloud-topped Mixed Layer Model', *J. Atmos. Sci.* **33**, 436–446.

Sommeria, G.: 1976, 'Three-Dimensional Simulation of Turbulent Processes in an Undistrubed Trade Wind Boundary Layer', *J. Atmos. Sci.* **33**, 216–241.

Sommeria, G. and Deardorff, J. W.: 1977, 'Subgrid-Scale Condensation in Models of Nonprecipitating Clouds', *J. Atmos. Sci.* **34**, 344–355.

Turner, J. S.: 1968, 'The Influence of Molecular Diffusivity on Turbulent Entrainment across a Density Interface', *J. Fluid Mech.* **23**, 639–656.

Willis, G. E. and Deardorff, J. W.: 1974, 'A Laboratory Model of the Unstable Planetary Boundary Layer', *J. Atmos. Sci.* **31**, 1297–1307.

Zeman, O. and Lumley, J. L.: 1976, 'Modeling Buoyancy Driven Mixed Layers', *J. Atmos. Sci.* **33**, 1974–1988.

Zeman, O. and Tennekes, H.: 1977, 'Parameterization of the Turbulent Energy Budget at the Top of the Daytime Atmospheric Boundary Layer', *J. Atmos. Sci.* **34**, 111–123.